frontiers in Physics

ORIGINAL RESEARCH
published: 14 June 2021
doi: 10.3389/fphy.2021.675375

Electronic Currents and Magnetic Fields in H_2^+ Induced by Coherent Resonant Bichromatic Circularly Polarized Laser Pulses: Effects of Orientation, Phase, and Helicity

André D. Bandrauk[1]*, *Szczepan Chelkowski*[1] and *Kai-Jun Yuan*[1,2†]

[1]Laboratoire de Chimie Théorique, Faculté des Sciences, Université de Sherbrooke, Sherbrooke, QC, Canada, [2]Institute of Atomic and Molecular Physics, Jilin University, Jilin, China

We theoretically study pulse phase and helicity effects on ultrafast magnetic field generation in intense bichromatic circularly polarized laser fields. Simulations are performed on the aligned molecular ion H_2^+ from numerical solutions of corresponding time-dependent Schrödinger equations. We demonstrate how electron coherent resonant excitation influences the phase and helicity of the optically induced magnetic field generation. The dependence of the generated magnetic field on the pulse phase arises from the interference effect between multiple excitation and ionization pathways, and is shown to be sensitive to molecular alignment and laser polarization. Molecular resonant excitation induces coherent ring electron currents, giving enhancement or suppression of the phase dependence. Pulse helicity effects control laser-induced electron dynamics in bichromatic circular polarization excitation. These phenomena are demonstrated by a molecular attosecond photoionization model and coherent electron current theory. The results offer a guiding principle for generating ultrafast magnetic fields and for studying coherent electron dynamics in complex molecular systems.

Keywords: magnetic field generation, intense laser pulses, coherent ring currents, multiple ionization pathways, bichromatic circularly polarized pulse

OPEN ACCESS

Edited by:
Robert Gordon,
University of Illinois at Chicago,
United States

Reviewed by:
Hirohiko Kono,
Tohoku University, Japan
Joern Manz,
Freie Universität Berlin, Germany

****Correspondence:***
André D. Bandrauk
Andre.Dieter.Bandrauk@usherbrooke.ca

†Deceased

Specialty section:
This article was submitted to Physical Chemistry and Chemical Physics, a section of the journal Frontiers in Physics

Received: *03 March 2021*
Accepted: *14 May 2021*
Published: *14 June 2021*

Citation:
Bandrauk AD, Chelkowski S and Yuan K-J (2021) Electronic Currents and Magnetic Fields in H_2^+ Induced by Coherent Resonant Bichromatic Circularly Polarized Laser Pulses: Effects of Orientation, Phase, and Helicity. Front. Phys. 9:675375. doi: 10.3389/fphy.2021.675375

1 INTRODUCTION

Imaging and manipulating molecular electron dynamics is one of the main goals in photophysical processes and photochemical reactions. Advances in synthesizing ultrashort intense laser pulses [1, 2] allow one to visualize and control electrons on their natural attosecond (1 as = 10^{-18} s) timescale and sub-nanometer dimension [3–6]. One important application of ultrashort circularly polarized attosecond pulses is to produce strong magnetic field pulses from electronic ring currents in atomic and molecular systems [7–13]. By creating unidirectional constant valence-type electronic currents in molecules with circularly polarized UV laser pulses, static magnetic fields [7–9] can be efficiently generated by the excitation of resonant degenerate orbitals. These laser-induced magnetic fields are much larger than those obtained by traditional static field methods [14]. In [8], it has been found that for the hydrogen-like atom, the existence of ring currents is related to the presence of the states having nonzero magnetic orbital momentum magnetic quantum numbers. Surprisingly, the strongest magnetic field originates from the $2p_{\pm}$ orbital in the hydrogen-like atom, which can

be prepared *via* resonant $1s \rightarrow 2p_{\pm}$ transition. One also finds that, in general, ring electronic currents are dependent on the symmetry of the molecular orbitals. The helicity of driving circularly polarized pulses [15] can be used to reconstruct attosecond charge migration [16–19]. Linearly polarized laser pulses can also induce excited ring currents by controlling the rotation direction of π electrons in planar/nonplanar aromatic molecules [20–22]. We have proposed methods previously to create "spinning" continuum electrons which can be generated and remain localized on sub-nanometer molecular dimensional scales [23, 24], offering a way to produce high-order harmonic generation (HHG). Time-dependent circular coherent electron wave packets (CEWPs) and currents are created as superposition of bound-continuum states. They thus become the source of intense time-dependent internal magnetic fields generated on attosecond timescale. The induced attosecond magnetic fields have been shown to be a function of various laser pulse parameters, such as the pulse intensity, wavelength, and duration [25, 26], thus providing new tools for control of ultrafast optical magnetism generation [27–31].

Investigating ultrafast electron dynamics by bichromatic circularly polarized attosecond laser pulses with corotating or counter-rotating components has been attracting considerable attention in the field of light–matter interactions. It has already been shown that counter-rotating intense ultrafast circularly polarized pulses can induce re-collision, thus ensuring efficient HHG [32–35], the new source of circularly polarized X-ray attosecond pulses. These counter-rotating laser fields are now being adopted to produce circularly polarized HHG with nonzero initial angular momenta [36–38]. With counter-rotating circularly polarized laser pulses, the technique of double optical gating can be efficiently employed for producing isolated elliptically polarized attosecond pulses [39]. Bichromatic laser fields have also been adopted to probe atomic and molecular structure by photoelectron momentum distributions [40]. By combination of two circularly polarized attosecond ultraviolet (UV) pulses, spiral electron vortices in photoionization momentum distributions have been predicted theoretically in both atomic [41–43] and molecular systems [44–46], which are shown to be sensitive to the helicity of the bichromatic fields. Recent experiments have demonstrated this fact by focusing on multiphoton femtosecond ionization of potassium atoms [47, 48]. Most recently, above-threshold ionization obtained previously by a bicircular field has been reported [49–52].

In this work, we present attosecond magnetic field generation and electron currents under molecular resonant excitation in bichromatic attosecond circular polarization processes. Such ultrafast attosecond pulses have been generated by current laser techniques from circularly polarized HHG [53–55]. Numerical simulations are performed on the aligned molecular ion H_2^+ at equilibrium by numerically solving the corresponding three-dimensional (3D) time-dependent Schrödinger equation (TDSE). Ultrafast magnetic field generation has been studied previously by bichromatic circularly polarized laser pulses [56, 57]. It has shown that the interference effect between multiple ionization pathway influences the magnetic field generation.

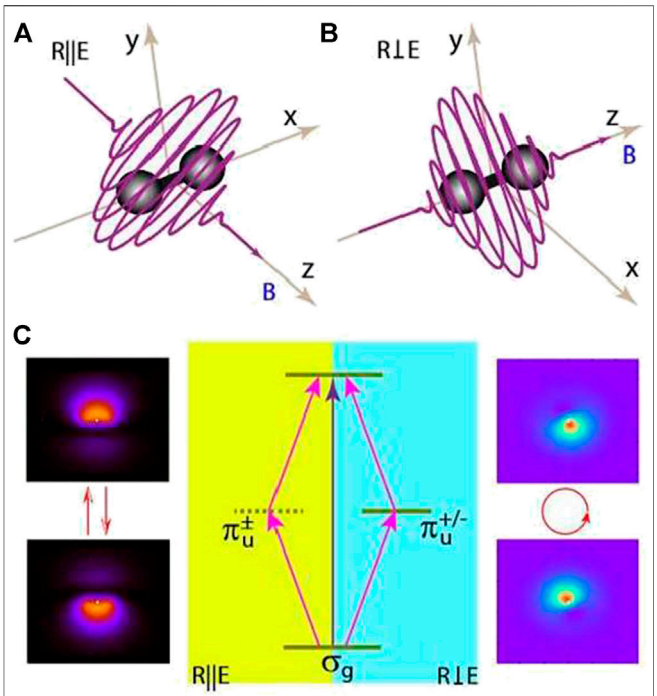

FIGURE 1 | Illustration of ultrafast magnetic field generation **B** under resonant excitation of H_2^+ aligned along the *x*/*z* axis by bichromatic co- and counter-rotating circularly polarized XUV pulses $\mathbf{E}(t)$ with their field vectors polarized in the (x, y) plane. Two excitation processes for the molecule axis parallel and perpendicular to the laser (x, y) polarization plane, that is, **(A)** in plane $\mathbf{R} \parallel \mathbf{E}$ and **(B)** around axis $\mathbf{R} \perp \mathbf{E}$, are compared. **(C)** Molecular $\sigma_g - \pi_u^{\pm}$ resonant excitation and ionization are shown for different molecular alignments, and corresponding evolutions of coherent electron wave packet density distributions at different times. Protons are at ±R/2 = ±1 a.u.

However, the effect of the coherent electron currents in bicircular magnetic field processes under molecular resonant excitation has not been presented. We focus here on the pulse phase and helicity-dependent magnetic field generation. We demonstrate molecular resonant excitation effects by comparing the dependence of the generated ultrafast magnetic field on the relative carrier-envelope phase (CEP) and the helicity of pulses at different molecular alignments. It is also found that attosecond charge migration arising from coherent resonant excitation induces coherent electron ring currents in molecules, leading to an absence of the CEP dependence. Induced electron ring currents resulting from molecular coherent resonant excitation are shown to be an important factor in bichromatic magnetic field generation. These results allow to control ultrafast magnetic fields, leading to molecular attosecond charge migration dynamics. Since molecular vibrational and rotational effects occur on the femtosecond ($1\,\text{fs} = 10^{-15}\,\text{s}$) and picosecond ($1\,\text{ps} = 10^{-12}\,\text{s}$) timescales, fixed nuclei simulations are valid and used to describe ultrafast magnetic field generation processes on the attosecond timescale.

The article is organized as follow: We briefly describe the computational method for solving TDSEs of the aligned molecular ion H_2^+ to simulate electron currents and magnetic field generation in **Section 2**. The results of ultrafast magnetic

fields by intense bichromatic circularly polarized attosecond XUV laser pulses are presented and discussed in **Section 3**. In **Section 4**, we finally summarize our findings. Throughout this article, atomic units (au) which are defined by setting $\hbar = e^2 = m_e = 1$ are used unless otherwise stated.

2 NUMERICAL METHODS

For the aligned molecule ion H_2^+ within Born–Oppenheimer approximation static nuclear frames, the corresponding 3D TDSE in the cylindrical coordinate $\mathbf{r} = (\rho, \theta, z)$ reads as

$$i\frac{\partial}{\partial t}\psi(\mathbf{r},t) = \left[-\frac{1}{2}\nabla_r^2 + V_{en}(\mathbf{r},\mathbf{R}) + V_L(\mathbf{r},t)\right]\psi(\mathbf{r},t), \quad (1)$$

with the Laplacian

$$-\frac{1}{2}\nabla_{\mathbf{r}}^2 = -\frac{1}{2\rho}\frac{\partial}{\partial\rho}\left(\rho\frac{\partial}{\partial\rho}\right) - \frac{1}{2\rho^2}\frac{\partial^2}{\partial\theta^2} - \frac{1}{2}\frac{\partial^2}{\partial z^2}, \quad (2)$$

where $V_{en}(\mathbf{r},\mathbf{R})$ is the electron-nuclear potential in which we fixed the internuclear separation to the equilibrium separation and $|\mathbf{R}| = 2$ au. The circularly polarized laser pulse propagates along the z axis, perpendicular to the (x,y) plane, with $x = \rho\cos\theta$ and $y = \rho\sin\theta$, as shown in **Figure 1**. The radiative interaction between the laser field and the electron $V_L(\mathbf{r}) = \mathbf{r}\cdot\mathbf{E}(t)$ is described in the length gauge for circularly polarized pulses of frequencies ω_1 and ω_2.

$$\begin{aligned}\mathbf{E}(t) &= \mathbf{E}_1(t) + \mathbf{E}_2(t)\\ &= Ef(t)\begin{cases}\hat{e}_x\left[\cos(\omega_1 t+\phi_1) + \cos(\omega_2 t+\phi_2)\right]\\ \hat{e}_y\left[\sin(\omega_1 t+\phi_1) + \epsilon\sin(\omega_2 t+\phi_2)\right]\end{cases},\end{aligned} \quad (3)$$

where $\hat{e}_{x/y}$ is the laser polarization direction, and the symbol $\epsilon = \pm 1$ denotes the helicity of combined fields, that is, corotating ($\epsilon = +1$) or counter-rotating ($\epsilon = -1$) components. ϕ_1 and ϕ_2 are CEPs of the pulses $\mathbf{E}_1(t)$ and $\mathbf{E}_2(t)$, respectively. A smooth $\sin^2(\pi t/T_{lp})$ pulse envelope $f(t)$ for maximum amplitude E, intensity $I = I_x = I_y = c\varepsilon_0 E^2/2$, and duration $T_{lp} = n\tau$ is adopted, where one optical cycle period $\tau_{1,2} = 2\pi/\omega_{1,2}$.

The 3D TDSE in **Eq. 1** is propagated by a second-order split operator method which conserves unitarity in each time step Δt combined with a fifth-order finite difference method and Fourier transform technique in the spatial steps $\Delta\rho$, Δz, and $\Delta\theta$ [59, 60]. The initial electron wave function $\psi(\mathbf{r}, t = 0)$ is prepared in the ground $1s\sigma_g$ state calculated by propagating an initial appropriate wave function in imaginary time using the zero-field TDSE in **Eq. 1**. The time step is taken to be $\Delta t = 0.01$ au $= 0.24$ as. The spatial discretization is $\Delta\rho = \Delta z = 0.25$ au for a radial grid range $0 \le \rho \le 128$ au (6.77 nm) and $|z| \le 32$ au (1.69 nm), and the angle grid size $\Delta\theta = 0.025$ radian. To prevent unphysical effects due to the reflection of the wave packet from the boundary, we multiply $\psi(\rho,\theta,z,t)$ by a "mask function" or absorber in the radial coordinate ρ with the form $\cos^{1/8}[\pi(\rho-\rho_a)/2\rho_{abs}]$. For all results reported here, we set the absorber domain at $\rho_a = \rho_{max}-\rho_{abs} = 104$ au with $\rho_{abs} = 24$ au, exceeding well the field-induced electron oscillation $\alpha_d = E/\omega_{1/2}^2$ of the electron [25]. The time-dependent probability current density is defined by the quantum expression in the length gauge,

$$\mathbf{j}(\mathbf{r},t) = \frac{i\hbar}{2m_e}\left[\psi(\mathbf{r},t)\nabla_{\mathbf{r}}\psi^*(\mathbf{r},t) - \psi^*(\mathbf{r},t)\nabla_r\psi(\mathbf{r},t)\right], \quad (4)$$

where $\psi(\mathbf{r},t)$ is the exact Born–Oppenheimer (static nuclei) electron wave function obtained from the TDSE in **Eq. 1**, and $\nabla_{\mathbf{r}} = e_\rho\nabla_\rho + e_\theta\nabla_\theta/\rho + e_z\nabla_z$ is the momentum operator in cylindrical coordinates. Then the corresponding *time-dependent* magnetic field is calculated using the following classical Jefimenko equation [61]:

$$\mathbf{B}(\mathbf{r},t) = -e\frac{\mu_0}{4\pi}\int\left[\frac{\mathbf{j}(\mathbf{r}',t_r)}{|\mathbf{r}-\mathbf{r}'|^3} + \frac{1}{|\mathbf{r}-\mathbf{r}'|^2 c}\frac{\partial\mathbf{j}(\mathbf{r}',t_r)}{\partial t}\right]\times(\mathbf{r}-\mathbf{r}')d^3\mathbf{r}', \quad (5)$$

where $t_r = t - r/c$ is the retarded time and $\mu_0 = 4\pi\times10^{-7}$ NA^{-2} (6.692×10^{-4} au) is the permeability of free space. Units of $B(\mathbf{r},t)$ are teslas (1 T = 10^4 Gauss) if the elementary charge e is in Coulombs. For the static zero-field time-independent conditions occurring after the pulse duration, **Eq. 5** reduces to the classical Biot–Savart law, that is, $B(\mathbf{r},t) = -e(\mu_0/4\pi)(v\times r)/r^3$ [61]. Note that the retardation effects due to r/c = 0.35 attoseconds (where for an estimate r = R = 2 au. is used) are negligible.

Of note is that equation **Eq. 4** defines the quantum probability current (not the electric current) as defined in any quantum mechanics textbook. The electron electric current used in the Biot–Savart law in **Eq. 5** is therefore $\mathbf{j}_{\text{electric}} = -e\mathbf{j}$. This explains the sign (−) in **Eq. 5**, e = 1 in atomic units.

3 RESULTS AND DISCUSSIONS

The ground and excited states of H_2^+ ion and its electron potentials, $1s\sigma_g$, $1s\sigma_u$, $2s\sigma_g$, $2s\sigma_g$, $1\pi_u$, *etc.*, are well documented in [65]. Numerical solutions of the TDSE for H_2^+ aligned with the laser polarization (x–y) plane, that is, $\mathbf{R} \parallel$ to the x-axis with the electric field vector $\mathbf{E}(t)$ rotating in the (x,y) plane (**Figure 1A**), are used for obtaining time-dependent probabilities P(t) of the $1s\sigma_g$ and $2p\pi_u$ states at equilibrium R = 2 au. excited by a 70-nm pulse at two different intensities, $I = 2\times10^{14}$ W/cm^2 and $I = 1\times10^{15} I = 1\times10^{15}$ W/cm^2, by a five-cycle pulse (one cycle = 0.234 fs = 234 as). Thus, at $I = 2\times10^{14}$, **Figure 2A**, one sees no significant ionization, whereas at $I = 1\times10^{15}$ W/cm^2, **Figure 2B**, the $2p\pi_u$ state is 85% occupied, and still one sees little ionization. In conclusion, short few-cycle intense and resonant pulses contribute little ionization with major excitation of the resonant state, such as the $2p\pi_u$ state at 70 nm and some Rydberg states above the $2p\pi_u$ state shown in 1.

We investigate laser-induced highly nonlinear optical effects using pairs of bichromatic circularly polarized laser pulses. We use $\lambda_1 = 70$ nm ($\omega_1 = 0.65$ au) circularly polarized pulse in combination with $\lambda_2 = 35$ nm ($\omega_2 = 2\omega_1 = 1.3$ au) circularly polarized pulse. Pairs of circularly polarized harmonics of different frequency and helicity can easily be prepared by a combination of pairs of counter-rotating circularly polarized laser pulses at different frequencies [62]. The molecular ion H_2^+ is aligned along the x/z axis, the two X-ray ultra violet (XUV) pulses with their field polarization vectors in the (x,y) plane propagate along the z axis, as illustrated in **Figure 1A**, for

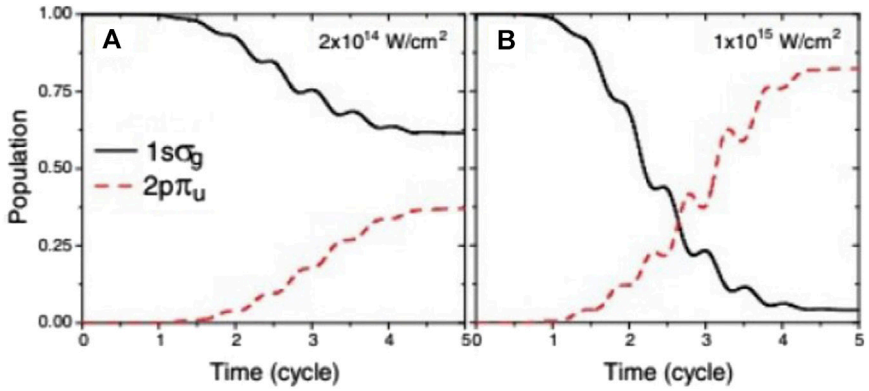

FIGURE 2 | Time-dependent probability density $\mathcal{D}(t)$ for in-plane excitation of (black solid line) the ground $1s\sigma_g$ state and of (red dashed line) the excited $2p\pi_u$ by λ_1 = 70 nm (ω_1 = 0.65 au) and 580 as FWHM circularly polarized UV laser pulses at two different pulse intensities: **(A)** $I = 2 \times 10^{14}$ W/cm^2 and **(B)** $I = 1 \times 10^{15}$ W/cm^2. 1-cycle = 234 as.

in-plane excitation, and **Figure 1B** for around axis excitation. With the pulse frequency$\omega_1 = \Delta E$ and the energy difference $\Delta E = E_{\pi_u} - E_{\sigma_g} = 0.65$ au, a resonant excitation with the ground $1s\sigma_g$ state and the excited π_u electronic states occurs. Moreover, with $\omega_2 = 2\omega_1$, such bichromatic laser pulses can also produce CEWPs with the same kinetic energies, $E_e = 2\omega_1 - I_p = \omega_2 - I_p$, by combination of multiple multiphoton transitions to Rydberg and the continuum state, thus leading to electron interference between the two ionization pathways. Since the induced electron currents are localized in the laser (x, y) polarization plane, the generated magnetic field is concentrated along the z axis. We therefore only present the results of the magnetic field B along the z axis.

As illustrated in **Figure 1C**, the coherent resonant excitation between the ground $1s\sigma_g$ state and the excited π_u state by the λ_1 = 70 nm circularly polarized laser pulse is dependent on the molecular alignment. In the case of $\mathbf{R} \parallel \mathbf{E}$, the in-plane degenerates perpendicular excitation, $\pi_u^{\pm} \leftarrow \sigma_g$ for different angular momenta $\Delta m = \pm 1$ dominates, and the electron density distribution evolves nearly perpendicular to the molecular axis [63], whereas in the case of $\mathbf{R} \perp \mathbf{E}$, the produced electron wave packets move around the molecular axis due to individual $\pi_u^{+/-} \leftarrow \sigma_g$ transitions $\Delta m = 1$ or -1 [64]. Meanwhile, two ω_1 and single ω_2 transitions to the continuum ($2\omega_1 = \omega_2 > I_p$) occur, leading to interference effects between these two excitation ionization channels. We show how coherent resonant excitation influences the interference effect on the magnetic field generation. We present the effects of the pulse phase on the attosecond magnetic field generation under the resonant excitation with various molecular alignments. Processes with different helicities ϵ, that is, corotating ($\epsilon = +1$) and counter-rotating ($\epsilon = -1$) pulse combinations, are compared as well.

3.1 Dependence of Generated Magnetic Fields on Circular Error Probability and Molecular Alignments

We first present the counter-rotating ($\epsilon = -1$) dynamics. **Figure 3** shows results of the generated maximum magnetic field B at the molecular center $\mathbf{r} = 0$ by intense single and bichromatic circularly polarized attosecond pulses described in **Eq. 3** [57]. Two cases of molecular excitation–ionization processes in the molecular ion H_2^+ aligned along a) the x axis, $\mathbf{R} \parallel \mathbf{E}$, and b) the z axis, $\mathbf{R} \perp \mathbf{E}$, are compared for the bichromatic laser pulses with their field polarization vectors in the (x,y) plane, as illustrated in **Figure 1**. The corresponding generated magnetic fields mainly lie in both cases along the z axis. The pulse wavelengths are, respectively, λ_1 = 70 nm (ω_1 = 0.65 au) and λ_2 = 35 nm (ω_2 = 1.3 au). We always fix the pulse intensities $I = 1 \times 10^{14}$ W/cm^2 (E = 0.0534 au) and durations T_{lp} = 48.3 au = 1.16 fs, corresponding to 580 as FWHM (full width at half maximum), that is, $5\tau_1$ for ω_1 pulse and $10\tau_2$ for ω_2 pulse. We also set the pulse CEP $\phi_1 = 0$ and vary the CEP ϕ_2 from 0 to 2π, that is, the relative CEP is $\phi = \phi_2 - \phi_1 = \phi_2$. **Figure 3** shows the CEP ϕ dependence of the generated magnetic fields with different molecular alignments.

3.1.1 Resonant Excitation in the Case of In-Plane R ∥ E

For the case of in-plane excitation with the molecule axis parallel to the laser (x, y) polarization plane as shown in **Figure 1A**, the generated magnetic field B at the molecular center is critically sensitive to the relative pulse CEP ϕ, as shown in **Figure 3A**. It is found that as the CEP ϕ varies from 0 to 2π, B oscillates periodically as $\cos(\phi)$. The maximum and minimum values of the magnetic field are B = 0.225 T and 0.165 T at $\phi \approx 0$ (or 2π) and π, respectively. For comparison, we also simulate the results of the induced magnetic field B with single-color circularly polarized attosecond pulses at separated wavelengths λ = 70 and 35 nm. The other parameters are the same as those used in **Figure 3A**. For the two single-pulse processes, the corresponding maximum strengths of induced magnetic fields at the molecular center are, respectively, $B^{\parallel}_{\omega_1} = 0.194$ T and $B^{\parallel}_{\omega_2} = 0.022$ T. Due to the $\sigma_g - \pi_u^+$ resonant excitation, the magnetic field induced by the resonant 70 pulse is much stronger than that induced by the nonresonant 35-nm pulse, $B^{\parallel}_{\omega_1} \approx 8.8 B^{\parallel}_{\omega_2}$. The sum value of the generated magnetic fields $B^{\parallel}_s = B^{\parallel}_{\omega_1} + B^{\parallel}_{\omega_2}$ is slightly smaller than the

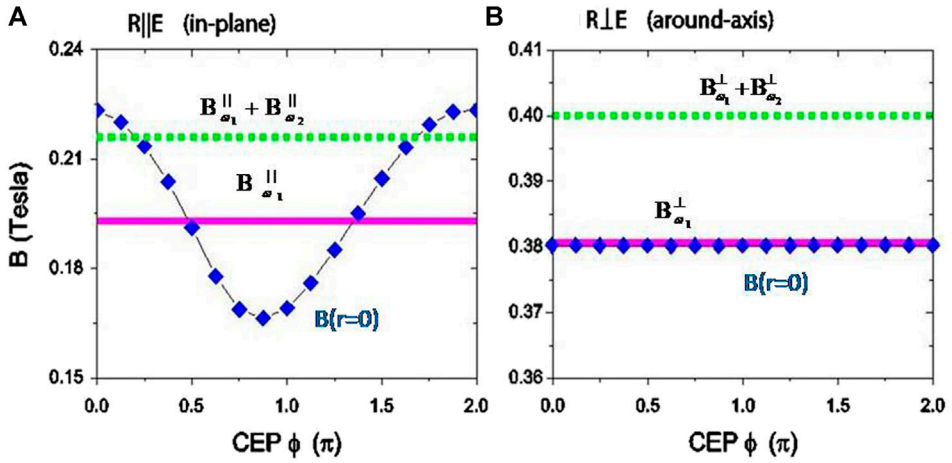

FIGURE 3 | Maximum magnetic fields B (**r** = 0) (blue diamond) at the molecular center as a function of CEP $\phi = \phi_2 - \phi_1$ for the aligned molecule H_2^+ in bichromatic counter-rotating ($\epsilon = -1$) circularly polarized laser pulses with their field vectors polarized in the (x, y) plane. Two cases are compared for the molecule aligned along **(A)** the x axis, in plane **R** ∥ **E**, and **(B)** the z axis, around axis **R** ⊥ **E**. Pulse wavelengths $\lambda_1 = 70$ nm ($\omega_1 = 0.65$ au) and $\lambda_2 = 35$ nm ($\omega_2 = 1.3$ au), intensities $I = 1 \times 10^{14}$ W/cm^2 ($E = 0.0534$ au), and duration $T_{lp} = 5\tau_1 = 10\tau_2$ (580 as FWHM) are fixed. Red solid lines denote the generated magnetic field $B^{\parallel}_{\omega_1} = 0.194$ T and $B^{\perp}_{\omega_1} = 0.382$ T by a single $\lambda = 70$ nm circularly polarized laser pulse, and green dashed lines present the sum values of the magnetic fields $B^{\parallel}_S = B^{\parallel}_{\omega_1} + B^{\parallel}_{\omega_2} = 0.216$ T and $B^{\perp}_S = B^{\perp}_{\omega_1} + B^{\perp}_{\omega_2} = 0.401$ T.

maximum field $B = 0.225$ T of the bicircular process. Comparing to the single-color circular processes, one notes that the sensitivity of the induced magnetic field B to the CEP ϕ in **Figure 3A** results from the interference effects between $\lambda_1 = 70$ nm and $\lambda_2 = 35$ nm optical processes.

From **Eq. 4**, **5**, for a simple ring current flowing in the ring having the radius r, one can derive a simple relation:

$$B \sim \mathcal{D}v/r^2, \tag{6}$$

where $\mathcal{D}$ is the probability density and v is the electron speed. This simple relation can be obtained in the following way: from the quantum definition of the current given in **Eq. 4** in which we assume that ψ is the plane wave, that is, $\psi = \sqrt{\mathcal{D}}\exp(i\mathbf{p}\cdot\mathbf{r}/\hbar)$, where **p** is the electron momentum tangent to the ring, one gets after performing the ∇ derivation a simple relation $j = D\frac{p}{m_e} = Dv$ as shown in [58]. Next, for the case of the electron current mainly localized in a plane one gets from **Eq. 5**, that is, $B \sim j/r^2 \sim \mathcal{D}v/r^2$, we thus derived **Eq. 6**.

Thus, in **Eq. 6**, the magnetic field is proportional to the electron probability density $\mathcal{D}$ and the electron velocity which originates from the electron current density $j = \mathcal{D}v$ [58]. Density $\mathcal{D}$ for the case of resonant transitions corresponds to the excited state transition probability, which is determined by the intrinsic transition dipole of molecules and the electric field strength as discussed in detail in **Supplementary Appendix A2**. Therefore, the dependence of the generated magnetic field in **Figure 3** on the pulse CEP ϕ mainly comes from the transition probability $\mathcal{D}$ which is influenced by the interference effect between color $\lambda_1 = 70$ nm and $\lambda_2 = 35$ nm pulse nonlinear optical responses, as presented in **Supplementary Appendix A1**.

With the bichromatic counter-rotating circularly polarized pulse at $\lambda_1 = 70$ nm and $\lambda_2 = 35$ nm, two nonlinear responses can be triggered. By the $\lambda_1 = 70$ nm pulse, resonance-enhanced excitation ionization occurs where the molecule is resonantly excited from the σ_g state to the degenerate $\pi_u^{\pm}$ state with $\omega_1 = E_e - E_g$ *via* a perpendicular transition. Meanwhile, the absorptions of two ω_1 photons and one $\omega_2 = 2\omega_1$ photon give rise to photoelectron wave packets with the same kinetic energies E_e in the continuum. The total photoionization probability is the sum of the two ionization excitation processes and their interference. As shown in **Supplementary Appendix A1**, the two ionization probabilities $\mathcal{D}^{(1)}$ and $\mathcal{D}^{(2)}$ are insensitive to the pulse phases, whereas the interference term $\mathcal{D}^{(1,2)}$ depends on the relative phase of the laser pulses and on the relative phase of the electron wave packets in the continuum. As a result, the total excitation probability density $\mathcal{D} = \mathcal{D}^{(1)} + \mathcal{D}^{(2)} + \mathcal{D}^{(1,2)}$ is also a cosine function of the relative pulse phase ϕ with the form $\mathcal{D} \sim \cos(\phi)$. The interference effect between the two processes modulates the total transition and current probabilities. Combining **Eq. 6** with Eqs 19 and 20 in **Supplementary Appendix A1**, one obtains $B \sim \cos(\phi)$, giving rise to a CEP dependence of the generated magnetic field, as illustrated in **Figure 3A** (blue diamond), B (r = 0).

3.1.2 Resonant Excitation in the Case of Around-Axis R ⊥ E

For around R axis excitation, **Figure 3B** shows phase-dependent magnetic field B generation in the process of molecule axis perpendicular to the laser (x, y) polarization plane, leading to around-axis currents. Comparing to the in-plane **R** ∥ **E** case in **Figure 3A**, one sees that the oscillation of the magnetic field B with the relative phase ϕ is, however, strongly suppressed. As shown in **Figure 3B**, the magnetic field is almost insensitive to the phase ϕ, with a constant value of $B = 0.38$ T. The magnetic fields generated by the individual bichromatic pulses are less than the sum of the two

single 70 and 35 nm processes, that is, $B < B_s^{\perp} = B_{\omega_1}^{\perp} + B_{\omega_2}^{\perp} = 0.4$ T, where $B_{\omega_1}^{\perp} = 0.382$ T and $B_{\omega_2}^{\perp} = 0.019$ T. The bichromatic magnetic fields mainly arise from the single-photon 70 nm process, $B = B_{\omega_1}^{\perp}$, whereas the contribution from the absorption of single 35 nm (ω_2) or two 70 nm (ω_1) photons is weak and negligible, as shown in **Figure 3B**. This implies that the interference effect between the two ionization processes does not influence the bichromatic magnetic field generation. Of note is that for the single ω_1/ω_2 pulse case, the generated magnetic fields are also dependent on the molecular alignments and the pulse wavelength. At $\lambda = 70$ nm, $B_{\omega_1}^{\perp} \approx 2B_{\omega_1}^{\parallel}$, the perpendicular case is stronger, whereas at 35 nm, the generated magnetic fields are nearly equivalent, $B_{\omega_2}^{\perp} \approx B_{\omega_2}^{\parallel}$. The difference indicates essentially the importance of the around R axis ring electron currents in the resonant intermediate π_u electronic state.

For the optical responses in **Figure 3B** of the molecule H_2^+ perpendicular to the laser (x, y) polarization plane, $\mathbf{R} \perp \mathbf{E}$, **Figure 1B**, by a single 70-nm circularly polarized pulse, resonant excitation between the ground σ_g state and the excited π_u^+ state with magnetic quantum number $\Delta m = 1$ leads to ring electron currents in molecules [64, 67]. As shown in **Supplementary Appendix A2**, using the electronic angular continuity equation [16, 17],

$$\frac{d}{dt}\mathcal{D}(\mathbf{r}, t) + \frac{d}{d\theta} j_{\theta}^{\perp}(\mathbf{r}, t) = 0. \tag{7}$$

One obtains the laser-induced electron current $j_{\theta}^{\perp}(r, t)$ in the following form

$$j_{\theta}^{\perp}(\mathbf{r}, t) \sim \cos(\Delta E t + \theta). \tag{8}$$

Eq. 8 combined with Eqs. 21 and 26 shows that for the superposition electron state $\psi_c(r, t)$, the time-dependent electronic density $\mathcal{D}(r, t)$ and the induced angular current $j_{\theta}^{\perp}(r, t)$ evolve in time with the electron coherence period of $\Delta\tau^{(0)} = 2\pi/\Delta E$. Therefore, the total magnetic field B in the bichromatic circularly laser field is mainly generated from the electron currents in the coherent electron wave packet $\psi_c(r, t)$ in Eq. 21 by the λ =70 nm pulse. The contributions from the continuum electron wave packets with energy E_e by the 35-nm pulse are clearly very weak, that is, $B_{\omega_1}^{\perp} \approx 20B_{\omega_2}^{\perp}$, and therefore negligible. As a result, altering the relative CEP ϕ does not lead to a variance of the generated magnetic field B.

3.1.3 Laser-Induced Electron Currents in Molecules

For the magnetic field B generated by coherent electron currents in molecules, the evolution of the induced electron currents $j_{\theta}(\mathbf{r}, t)$ with time t is determined by the coherent resonant excitation and the molecular alignments. **Figure 4** illustrates snapshots of angular electron probability currents $j_{\theta}^{\perp}(x, y, z = 0, t)$ at the center of H_2^+ obtained from **Eq. 4** at different times t (unit of $\tau = 2\pi/\omega_1 = \tau_1$) for the molecule H_2^+ perpendicular to the laser (x, y) polarization plane, $\mathbf{R} \perp \mathbf{E}$, **Figure 1**, leading to around R axis currents, $j_{\theta}^{\perp}(x, y, z = 0, t) = j_{\theta}^{\perp}(\rho\cos\theta, \rho\sin\theta, z = 0, t)$. The bichromatic counter-rotating ($\epsilon = -1$) circularly polarized XUV pulse at CEPs $\phi_1 = \phi_2 = 0$ is used to excite the molecule. It is found that the induced electron currents are asymmetric with respect to the molecular center and rotate with a period of τ around the z or molecular R axis in the (x, y) polarization plane with an anticlockwise direction, as predicted in **Eq. 8**. This confirms that the ring electron currents mainly arise from the coherent resonant excitation between the ground σ_g state and the excited π_u^+ state by the 70-nm circularly polarized pulse [64]. From such coherent electron currents, the generated magnetic fields are unidirectional, along the z/R axis. At the molecular center $z = 0$, the magnetic field is the sum of those at the two nuclei, $\pm R/2$. In the bichromatic circular polarized processes, the contributions of the magnetic field generation from the 70 nm pulse are dominant, which do not depend on the pulse phase. Therefore, varying the relative pulse CEP ϕ does not influence the generated magnetic field B, as illustrated in **Figure 3B**.

For comparison, in **Figure 5**, we also plot the in-plane electron probability current $j_{\theta}^{\parallel}(x, y, z = 0, t)$ at the center of the molecule H_2^+ aligned along the x axis, parallel to the laser polarization (x, y) plane, $\mathbf{R} \parallel \mathbf{E}$ in **Figure 1A**, of bichromatic counter-rotating circularly polarized pulses. Combining **Figure 4** with **Figure 5**, one sees that these time-dependent electron currents are sensitive to the molecular alignments. The joint $\sigma_g - \pi_u^{\pm}$ resonant excitations induce coherent electron currents. The induced electron probability currents are mainly localized along the molecular internuclear axis, that is, the resonant perpendicular atomic ($p_y \leftarrow s$) transitions dominate during the excitation processes. In this case, the coherent exited electronic state is given by

$$\pi_u^c(\mathbf{r}) = -i\left[\pi_u^+(\mathbf{r}) - \pi_u^-(\mathbf{r})\right]/2 = \pi_u^y(\mathbf{r}), \tag{9}$$

where $\pi_u^{\pm}(\mathbf{r}) = [\pi_u^x(\mathbf{r}) \pm i\pi_u^y(\mathbf{r})]/\sqrt{2}$ and $|\tilde{\pi}_u^{\pm}(\mathbf{r})|^2 = [|\pi_u^x(\mathbf{r})|^2 + |\pi_u^y(\mathbf{r})|^2]/2$. Then the corresponding interference term in the time-dependent electron density becomes (in cylindrical coordinates (ρ, θ, z) as shown in [9, 64] and in **Supplementary Appendix A2**)

$$\mathcal{D}_{(e,g)}(r, t) = 2c_g c_e \psi_g(r)\tilde{\psi}_e^{\pm}(\rho, z)\cos(\Delta E t)\sin(\theta), \tag{10}$$

and the time-dependent current

$$j_{\theta}^{\parallel}(r, t) = -2c_g c_e \psi_g(r)\tilde{\psi}_e^{\pm}(\rho, z)\Delta E \sin(\Delta E t)\cos(\theta), \tag{11}$$

where $\tilde{\psi}_e^{\pm}(\rho, z)$ is the absolute value of $\psi_e^{\pm}$ (see Eq. 23). It is found that the coherent density and current superposition terms in **Eqs. 10** and **11** follow the forms $\sim\sin(\theta)$ and $\cos(\theta)$. As a result, the coherent wave packets due to the $\sigma_g - \pi_u^{\pm}$ superposition oscillate along the y direction, perpendicular to the molecular axis, **Figure 1C**, whereas the corresponding currents oscillate mainly along the molecular axis, **Figure 4**. The generated magnetic field at the two molecular nuclear centers $\pm R/2$ has opposite phases [70]. Their overlap leads to a weak magnetic field at the molecule center $z = 0$. The generated magnetic field in **Figure 3A** therefore mainly results from the coherent excitation by bichromatic circularly polarized laser pulses.

3.2 Influence of the Pulse Helicity

We next study the process with a bichromatic corotating ($\epsilon = +1$) circularly polarized laser pulse. **Figure 6** shows the maximum generated magnetic field B at various relative pulse phases ϕ. The other laser parameters are the same as those

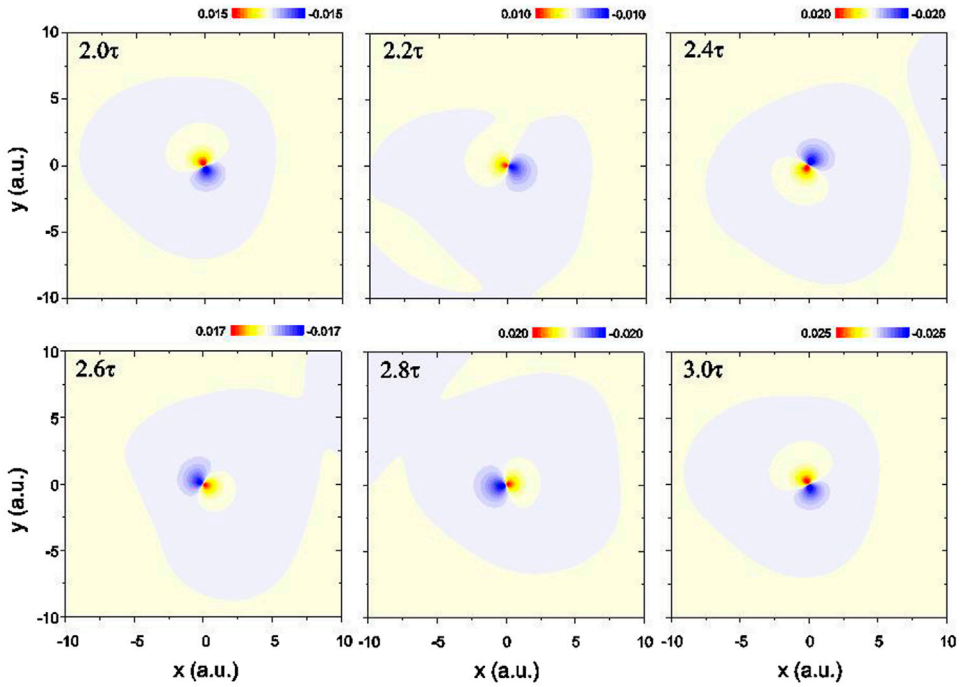

FIGURE 4 | Evolutions of the induced angular electron probability current density $j_\theta^\perp(x,y,z=0,t)$ at different times t (unit of $\tau=\tau_1=2\pi/\omega_1$) for the molecule perpendicular to the laser polarization (x,y) plane, that is, around-axis $\mathbf{R}\perp\mathbf{E}$, by bichromatic counter-rotating ($\epsilon=-1$) circularly polarized laser pulses at wavelengths $\lambda_1=70$ nm ($\omega_1=0.65$ au) and $\lambda_2=35$ nm ($\omega_2=1.3$ au), intensities $I=1\times10^{14}$ W/cm^2 (E = 0.0534 au), duration $T_{lp}=5\tau_1=10\tau_2$ (580 as FWHM), and relative CEP $\phi=0$. Units of induced angular electron currents are arbitrary.

used in **Figure 3**. It was found that similar results are obtained in **Figure 6**, as the counter-rotating ($\epsilon=-1$) case in **Figure 3**. For the case of $\mathbf{R}\parallel\mathbf{E}$, the magnetic field B varies as a sine function of the phase ϕ, as predicted in **Supplementary Appendix A1**. A phase $\pi/2$ shift occurs in the CEP ϕ-dependent magnetic field generation by the corotating bichromatic pulses. This mainly results from the different electron dynamics induced by the two pulses with opposite helicity. It was also found for the corotating ($\epsilon=+1$) case the generated magnetic field depends on the molecular alignment. In **Figure 6B**, we see that for the case of $\mathbf{R}\perp\mathbf{E}$, the total generated magnetic field (blue diamond) is shown to be almost insensitive to the relative CEP ϕ, similar as in **Figure 3B**. At various pulse phases ϕ, the magnetic field $B=0.38$ T is obtained. The $\sigma_g-\pi_u^+$ resonant excitation with $\Delta m=1$ gives rise to unidirection ring electron currents, as illustrated in **Figure 3**. The contribution from the coherent electron wave packets $\psi_0(\mathbf{r},t)$ in Eq. 21 dominates. The effects of the multiple pathway ($2\omega_1$ and ω_2) excitation interference can be neglected. Consequently, the generated magnetic field does not depend on the pulse CEP ϕ. The independence of the generated magnetic field on the pulse helicity ϵ also confirms the importance of the charge migration. This offers an approach to explore molecular structure and orbitals.

It should be noted that in the case of $\mathbf{R}\parallel\mathbf{E}$ in the general pulse $\mathbf{E}(t)$ with its field polarization vectors in the (x,y) plane, the strength of the generated magnetic field is slightly sensitive to the pulse helicity ϵ. As shown in **Figure 6A**, at $\epsilon=+1$ for corotating cases, the maximum magnetic field is $B=0.206$ T at $\phi=0.4\pi$, which is slightly weaker than that at $\epsilon=-1$ for counter-rotating cases in **Figure 3A**, where $B=0.225$ T at $\phi=0$. **Eq. 6** predicts that the induced magnetic field, in general, is proportional to the ratio of the electron velocity v and inversely proportional to r^2, where r is the radius of the excitation state of an electron under the influence of a strong laser field. The difference between the corotating and counter-rotating generated magnetic fields in **Figures 3A**,**6A** results from the laser-induced dynamics, which depends on the helicity of driving pulses.

According to the classical laser-induced electron motion models [68, 69], the electron velocity and radius are determined by the pulse amplitude E, frequency $2\omega_1=\omega_2$, and helicity ϵ, which are given by

$$\dot{x}(t)=-\frac{E}{\omega_1}\left\{\sin(\omega_1 t)-\sin(\omega_1 t_0)+\frac{1}{2}\left[\sin(\omega_2 t)-\sin(\omega_2 t_0)\right]\right\},$$
$$\dot{y}(t)=-\frac{E}{\omega_1}\left\{\cos(\omega_1 t_0)-\cos(\omega_1 t)+\frac{\epsilon}{2}\left[\cos(\omega_2 t_0)-\cos(\omega_2 t)\right]\right\}, \tag{12}$$

and the corresponding electron displacements are

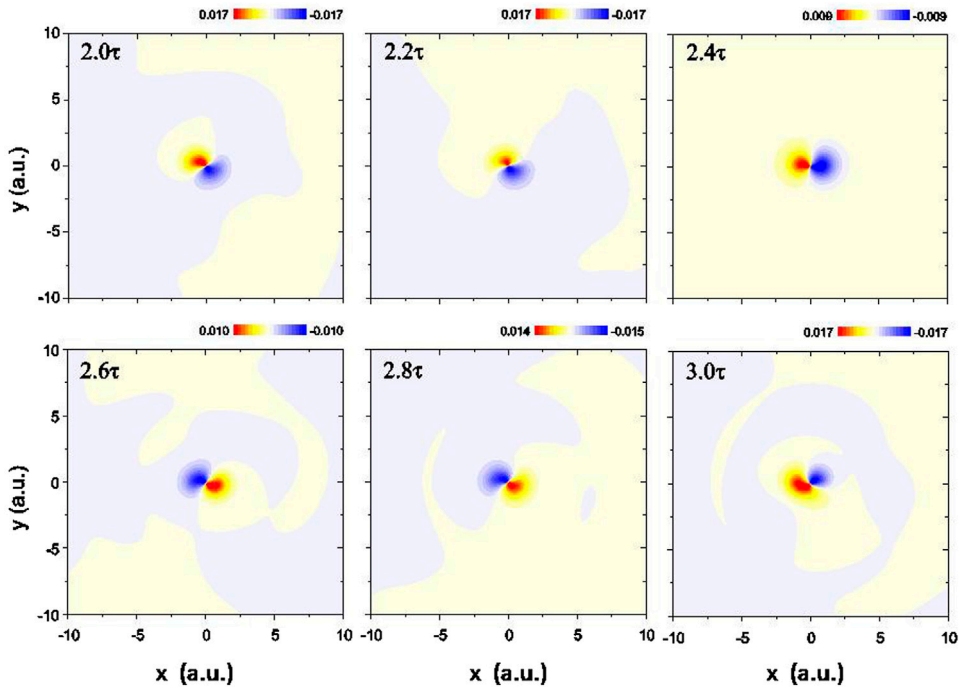

FIGURE 5 | Time dependence of the induced angular probability electron current $j_\theta^{\parallel}(x,y,z=0,t)$ at different moments t (unit of $\tau = \tau_1 = 2\pi/\omega_1$) for the molecular axis parallel to the laser polarization (x,y) plane, that is, in-plane **R** ∥ **E**, by bichromatic counter-rotating ($\epsilon = -1$) circularly polarized laser pulses at wavelengths $\lambda_1 = 70$ nm ($\omega_1 = 0.65$ au) and $\lambda_2 = 35$ nm ($\omega_2 = 1.3$ au), intensities $I = 1 \times 10^{14}$ W/cm^2 (E = 0.0534 au), duration $T_{lp} = 5\tau_1 = 10\tau_2$ (580 as FWHM), and CEP $\phi = 0$. Units of induced angular electron probability currents are arbitrary.

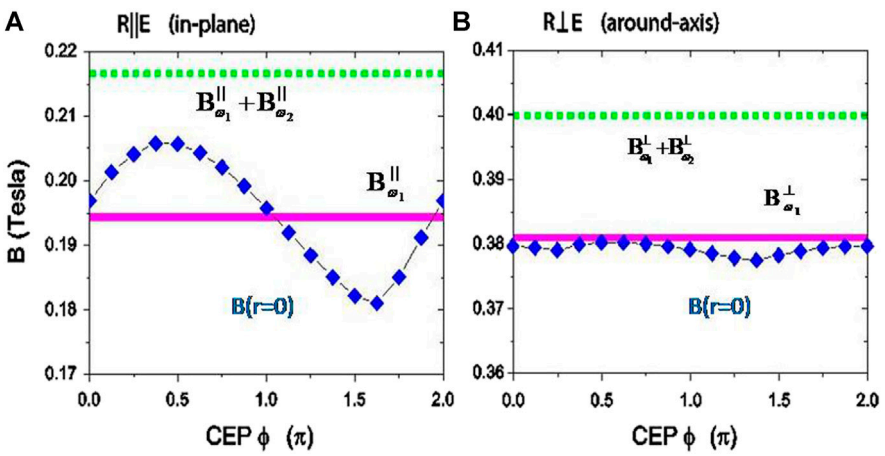

FIGURE 6 | Dependence of the maximum magnetic field B (blue diamond) at the molecular center, $r = 0$ on the relative pulse CEP $\phi = \phi_2 - \phi_1$ for the aligned molecule H_2^+ by bichromatic corotating ($\epsilon = +1$) circularly polarized laser pulses with their field vectors polarized in the (x,y) plane. Two cases are compared for the molecule aligned parallel to **(A)** the x axis and **(B)** the z axis, that is, parallel **R** ∥ **E** in **Figure 1A** and perpendicular **R** ⊥ **E** in **Figure 1B**, to the laser (x,y) polarization plane. Pulse wavelengths $\lambda_1 = 70$ nm ($\omega_1 = 0.65$ au) and $\lambda_2 = 35$ nm ($\omega_2 = 1.3$ au), intensities $I = 1 \times 10^{14}$ W/cm^2 ($E = 0.0534$ au), and duration $T_{lp} = 5\tau_1 = 10\tau_2$ (580 as FWHM) are fixed. Magenta solid lines denote the generated magnetic field $B^{\parallel}_{\omega_1} = 0.194$ T and $B^{\perp}_{\omega_1} = 0.382$ T by a single $\lambda = 70$ nm circularly polarized laser pulse, and green dashed lines are the sum values of the magnetic fields $B^{\parallel}_S = B^{\parallel}_{\omega_1} + B^{\parallel}_{\omega_2} = 0.216$ T and $B^{\perp}_S = B^{\perp}_{\omega_1} + B^{\perp}_{\omega_2} = 0.401$ T.

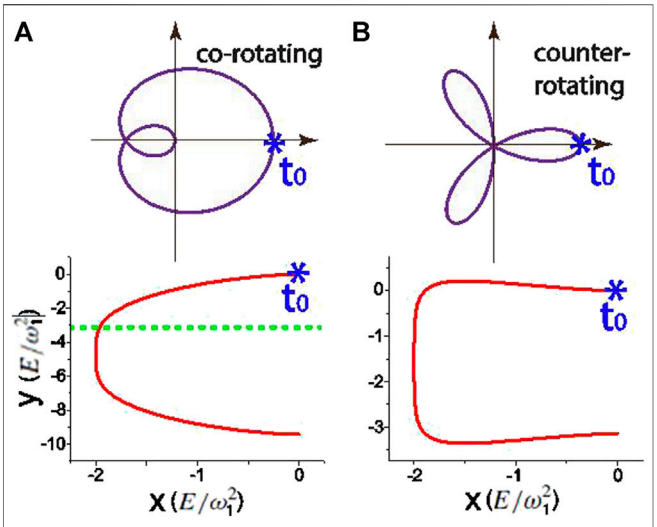

FIGURE 7 | Bichromatic ($\omega_2 = 2\omega_1$) circularly polarized (top row) electric field vectors and (bottom row) corresponding laser-induced displacement trajectories $[x(t), y(t)]$ of free electrons for **(A)** corotating ($\epsilon = +1$) and **(B)** counter-rotating ($\epsilon = -1$) helicity schemes. The initial position is $x(t_0) = y(t_0) = 0$, where t_0^* indicates the ionization time at the maxima of the combined fields. Green line corresponds to the minimum laser-induced radius r_0 of an ionized electron at frequency ω_1 and circular field amplitude E, $r_0 = (2E/\omega_1^2)\sqrt{1 + (\pi/2)^2}$ as shown in [23].

$$
\begin{aligned}
x(t) &= -\frac{E}{\omega_1^2}\{\cos(\omega_1 t_0) - \cos(\omega_1 t) - \omega_1 (t - t_0)\sin(\omega_1 t_0) \\
&+ \frac{1}{4}[\cos(\omega_2 t_0) - \cos(\omega_2 t) - \omega_2 (t - t_0)\sin(\omega_2 t_0)]\}, \\
y(t) &= -\frac{E}{\omega_1^2}\{\sin\omega_1 t_0 - \sin\omega_1 t + \omega_1 (t - t_0)\cos(\omega_1 t_0) \\
&+ \frac{\epsilon}{4}[\sin\omega_2 t_0 - \sin(\omega_2 t) + \omega_2 (t - t_0)\cos(\omega_2 t_0)]\},
\end{aligned}
\tag{13}
$$

where t_0 is the ionization time. **Figure 7** shows bichromatic circularly polarized laser field vectors with corotating and counter-rotating components and corresponding induced electron displacements, where zero initial position of one ionized electron is assumed, that is, $x(t_0) = y(t_0) = 0$. Such electron displacements can be measured by interfering spirals in photoelectron momentum distributions [71]. With the XUV pulses, a multiphoton ionization process occurs since the Keldysh parameter $\gamma > 1$ [72]. The initial electron velocities are nearly equivalent with $\sqrt{2(\omega_2 - I_p)}$. As shown in **Figure 7**, for the corotating $\epsilon = 1$ case, the radius of the continuum electron is much larger than that of the counter-rotating $\epsilon = -1$ case. The electron moves way quickly in the corotating field, whereas the counter-rotating field restricts the ionized electron around the molecular center. Because $B \sim j/r^2$ in **Eq. 5**, **6**, weaker maximum magnetic field is generated in the corotating case in **Figure 5A**. The dependence of generated magnetic fields on the pulse helicity ϵ reflects the laser-induced electron dynamics in bichromatic fields. The present simulation confirms that steering the radius of the induced electron currents allows to control generated magnetic fields with bichromatic circularly polarized pulses.

4 CONCLUSION

We present the ultrafast magnetic field generation in molecules from one electron molecular TDSE simulation under effects of coherent resonant excitation in bichromatic ($\omega_2 = 2\omega_1$) co- and counter-rotating circularly polarized laser fields. Numerical results are obtained for the aligned molecular ion H_2^+, which can be fully and exactly studied. We evaluate the generated magnetic field $B(\mathbf{r} = 0)$ at the molecular center at different relative CEP ϕ of the two circularly polarized pulses with both counter-rotating and corotating combinations. It is found that altering the CEP ϕ varies the maximum values of the generated magnetic field, $B(\mathbf{r} = 0)$, which is shown to be dependent on the molecule alignment, and is maximum for in-plane bichromatic excitation.

In a bichromatic (frequency $\omega_1 \neq \omega_2$) circularly polarized field, a $\sigma_g - \pi_u^{\pm}$ resonant excitation of individual magnetic components $m = \pm 1$ is triggered by the resonant ω_1 (70 nm) pulse. As a result, coherent electron currents between the ground σ_g state and the degenerate excited $\pi_u^{\pm}$ electronic state are induced in molecules. We compare two nonlinear responses for different molecular alignments:

- For the around-axis case, $\mathbf{R} \perp \mathbf{E}$, the molecule aligned along the z axis, perpendicular to the laser (x, y) polarization plane, **Figure 1B**, and the magnetic field mainly results from the coherent electron currents which are induced by one resonant ω_1 photon around R. The contribution from two ω_1 photons or one ω_2 photon is negligible. Varying the relative CEP ϕ does not influence the generated magnetic field. Similar results are obtained for both counter-rotating $\varepsilon = -1$, **Figure 3B**, and corotating $\varepsilon = +1$, **Figure 6B**, excitations, confirming the main role of the around-axis circular coherent electron current.
- For the in-plane case, $\mathbf{R} \parallel \mathbf{E}$, the molecule aligned parallel to the laser (x, y) polarization plane, **Figure 1A**, and the magnetic field generation is shown to be strongly dependent on the pulse phase ϕ, confirming the effects of multiple pathway ionization. The in-plane coherent electron currents generate the magnetic fields in the two nuclei with opposite phases and evolve perpendicular to the molecular R axis. Their superposition suppresses the magnetic field generation at the molecular center, **Figure 3**. The results we present arise mainly from the total electron currents by one ω_1 photon absorption, that is, the $\sigma_g - \pi_u^{\pm}$ resonant excitation, and two ω_1 or one ω_2 transition to the continuum. The generated magnetic field depends on the photoionization probability which is a function of the relative CEP ϕ Eq. 20. As a consequence of interference effects between the ω_1 and ω_2 photoionization pathways, altering their relative phase ϕ gives rise to a modulation of the generated magnetic field $B(\mathbf{r} = 0)$ at the molecular center with forms $\sim \cos(\phi)$ for counter-rotating and

$\sin(\phi)$ for corotating combinations. It is also shown that the maximum of the magnetic field for the counter-rotating case is larger than that for the corotating case because of the difference in laser-induced electron displacements, which depends strongly on the helicity of the driving pulse, **Figure 6**.

The present results in principle provide the importance of coherent electron dynamics and of control magnetic fields by bichromatic circularly polarized laser pulses. The dependence of the generated magnetic field on the relative phase and helicity of driving laser pulses also allows to characterize the property of laser pulses and probe coherent electron currents and to charge migration in molecules. Although a simple single electron molecular ion H_2^+ is used, similar electron dynamics phenomena should be predicted in more complex molecular systems [7, 27, 30, 73], thus offering an approach for controlling ultrafast magnetic field generation.

The above laser-induced molecular magnetic field generation on the electron's quantum timescale, the asec, was studied in the Born–Oppenheimer Approximation, that is, with static nuclei. Nuclear motion effects, that is, non–Born–Oppenheimer, are now being pursued on the near femtosecond timescale in order to include nuclear motion effects with bound and dissociation molecular states [83], de-and re-coherence in charge migration [84] and isotope effects in HD+ ultrafast ionization [85]. In the case of laser pulses propagating perpendicular to the molecular R-axis with the pulse electric fields in the molecular plane, **Figure 1A**, re-collision of electron currents with nuclei is an important nonlinear optical effect shown in **Figure 6** to be examined in detail for moving nuclei. Finally, the strong magnetic fields generated by intense ultrafast laser pulses are expected to interact with the electron currents themselves. Proton beams have been shown recently to be useful tools to measure intense magnetic field directions generated by current solenoids [86], thus confirming that laser-generated magnetic fields can interact also with nuclei in matter.

AUTHOR CONTRIBUTIONS

AB as a research leader directed this research formulated research goals and contributed in the scientific interpretation of results. KY wrote codes, executed codes, and prepared graphics but died last March before completing this research. SC participated in initial algorithm preparation for computer codes and did final preparation.

FUNDING

This work is supported in part by the National Natural Science Foundation of China (Grant Nos. 11974007 and 11574117) and the NSERC-RGPIN2019-05291.

ACKNOWLEDGMENTS

The authors also thank Compute Canada for access to massively parallel computer clusters, and the Natural Sciences and Engineering Research Council of Canada and the Fonds de Recherche du Québec-Nature et Technologies for supporting their research work.

SUPPLEMENTARY MATERIAL

The Supplementary Material for this article can be found online at: https://www.frontiersin.org/articles/10.3389/fphy.2021.675375/full#supplementary-material

REFERENCES

1. Krausz F., and Ivanov M. Attosecond Physics. *Rev Mod Phys* (2009) 81:163, 234. doi:10.1103/revmodphys.81.163
2. Chang Z., Corkum P. B., and Leone S. R. Attosecond optics and technology: progress to date and future prospects [Invited]. *J Opt Soc Am B* (2016) 33:1081. doi:10.1364/josab.33.001081
3. Chelkowski S., Yudin G. L., and Bandrauk A. D. Observing Electron Motion in Molecules. *J Phys B At Mol Opt Phys* (2006) 39:S409, S417. doi:10.1088/0953-4075/39/13/s14
4. Niikura H, Villeneuve DM, and Corkum PB. Mapping Attosecond Electron Wave Packet Motion. *Phys Rev Lett* (2005) 94:083003. doi:10.1103/physrevlett.94.083003
5. Shao HC, and Starace AF. Detecting Electron Motion in Atoms and Molecules. *Phys Rev Lett* (2010) 105:263201. doi:10.1103/physrevlett.105.263201
6. Vrakking M. J. J., and Elsaesser T.. X-rays inspire electron movies. *Nature Photon* (2012) 6:645, 647. doi:10.1038/nphoton.2012.247
7. Barth I., Manz J., Shigeta Y., and Yagi K.. Unidirectional Electronic Ring Current Driven by a Few Cycle Circularly Polarized Laser Pulse: Quantum Model Simulations for Mg–Porphyrin. *J Am Chem Soc* (2006) 128:7043, 7049. doi:10.1021/ja057197l
8. Barth I, and Manz J. Electric Ring Currents in Atomic Orbitals and Magnetic fields Induced by Short Intense Circularly Polarized π Laser Pulses. *Phys Rev A* (2007) 75:012510. doi:10.1103/physreva.75.012510
9. Barth I., Serrano-Andrés L., and Seideman T. Nonadiabatic Orientation, Toroidal Current, and Induced Magnetic Field in BeO Molecules. *The Journal of Chemical Physics* (2008) 129:164303. doi:10.1063/1.2994737
10. Barth I, and Manz J. Quantum Switching of Magnetic Fields by Circularly Polarized Optimized Laser Pulses. In: K Yamanouchi, G Gerber, and AD Bandrauk, editors. *Progress in Ultrafast Intense Laser Science VI*, 2021. Springer Verlag Berlin (2010) p. 2.
11. Barth I., Manz J., and Serrano-Andrés L. Quantum Simulations of Toroidal Electric Ring Currents and Magnetic fields in Linear Molecules Induced by Circularly Polarized Laser Pulses. *Chemical Physics* (2008) 347:263–271. doi:10.1016/j.chemphys.2007.09.037
12. Köksal K., and Koç F. The Effect of Twisted Light on the Ring-Shaped Molecules: The Manipulation of the Photoinduced Current and the Magnetic Moment by Transferring Spin and Orbital Angular Momentum of High Frequency Light. *Computational and Theoretical Chemistry* (2017) 1099:203, 208. doi:10.1016/j.comptc.2016.11.031
13. Zhang G, Murakami M, Lefkidis G, Hübner W, and George TF. *Introduction to Ultrafast , From Femtosecond Magnetism to High-Harmonic Generation*. CRC Press, Taylor & Francis Group (2020) doi:10.1201/9780429194832

14. Nobusada K, and Yabana K. Photoinduced Electric Currents in Ring-Shaped Molecules by Circularly Polarized Laser Pulses. *Phys Rev A* (2007) 75:032518. doi:10.1103/physreva.75.032518
15. Jia D., Manz J., Paulus B., Pohl V., Tremblay J. C., and Yang Y. Quantum Control of Electronic Fluxes during Adiabatic Attosecond Charge Migration in Degenerate Superposition States of Benzene. *Chemical Physics* (2017) 482:146, 159. doi:10.1016/j.chemphys.2016.09.021
16. Hermann G., Liu C., Manz J., Paulus B., Pérez-Torres J. F., Pohl V., et al. Multidirectional Angular Electronic Flux during Adiabatic Attosecond Charge Migration in Excited Benzene. *J Phys Chem A* (2016) 120:5360, 5369. doi:10.1021/acs.jpca.6b01948
17. Hermann G., Liu C., Manz J., Paulus B., Pohl V., and Tremblay J. C. Attosecond Angular Flux of Partial Charges on the Carbon Atoms of Benzene in Non-aromatic Excited State. *Chemical Physics Letters* (2017) 683:553, 558. doi:10.1016/j.cplett.2017.01.030
18. Ding H., Jia D., Manz J., and Yang Y. Reconstruction of the electronic flux during adiabatic attosecond charge migration in HCCI+. *Molecular Physics* (2017) 115:1813, 1825. doi:10.1080/00268976.2017.1287967
19. Jia D., Manz J., and Yang Y.. Generation of electronic flux during the femtosecond laser pulse tailored to induce adiabatic attosecond charge migration in. *Journal of Modern Optics* (2017) 64:960, 970. doi:10.1080/09500340.2016.1269216
20. Kanno M, Kono H, Fujimura Y, and Lin SH. Nonadiabatic Response Model of Laser-Induced Ultrafast π-electron Rotations in Chiral Aromatic Molecules. *Phys Rev Lett* (2010) 104:108302. doi:10.1103/physrevlett.104.108302
21. Mineo H., Lin S. H., and Fujimura Y. Coherent π-electron dynamics of (P)-2,2′-biphenol induced by ultrashort linearly polarized UV pulses: Angular momentum and ring current. *The Journal of Chemical Physics* (2013) 138:074304. doi:10.1063/1.4790595
22. Kanno M., Kono H., and Fujimura Y. Laser-Control of Ultrafast π-Electron Ring Currents in Aromatic Molecules: Roles of Molecular Symmetry and Light Polarization. *Applied Sciences* (2018) 8:2347. doi:10.3390/app8122347
23. Yuan K.-J., and Bandrauk A. D. Circularly polarized attosecond pulses from molecular high-order harmonic generation by ultrashort intense bichromatic circularly and linearly polarized laser pulses. *J Phys B At Mol Opt Phys* (2012) 45:074001. doi:10.1088/0953-4075/45/7/074001
24. Yuan KJ, Lu H, and Bandrauk AD. High-order-harmonic Generation in Molecular Sequential Double Ionization by Intense Circularly Polarized Laser Pulses. *Phys Rev A* (2015) 92:023415. doi:10.1103/physreva.92.023415
25. Yuan KJ, and Bandrauk AD. Attosecond-magnetic-field-pulse Generation by Intense Few-Cycle Circularly Polarized UV Laser Pulses. *Phys Rev A* (2013) 88:013417. doi:10.1103/physreva.88.013417
26. Yuan KJ, and Bandrauk AD. Attosecond-magnetic-field-pulse Generation by Coherent Circular Molecular Electron Wave Packets. *Phys Rev A* (2015) 91:042509. doi:10.1103/physreva.91.042509
27. Zhang G. P., Hübner W., Lefkidis G., Bai Y., and George T. F. Paradigm of the Time-Resolved Magneto-Optical Kerr Effect for Femtosecond Magnetism. *Nature Phys* (2009) 5:499, 502. doi:10.1038/nphys1315
28. Zhang GP, and George TF. Total Angular Momentum Conservation in Laser-Induced Femtosecond Magnetism. *Phys Rev B* (2008) 78:052407. doi:10.1103/physrevb.78.052407
29. Kim J-W, Vomir M, and Bigot J-Y. Ultrafast Magnetoacoustics in Nickel Films. *Phys Rev Lett* (2012) 109:166601. doi:10.1103/physrevlett.109.166601
30. Bigot J.-Y.. Down to the nanometre scale. *Nature Mater* (2013) 12:283, 284. doi:10.1038/nmat3605
31. Zhang X, Zhu X, Wang D, Li L, Liu X, Liao Q, et al. Ultrafast Oscillating-Magnetic-Field Generation Based on Electronic-Current Dynamics. *Phys Rev A* (2019) 99:013414. doi:10.1103/physreva.99.013414
32. Zuo T., and Bandrauk A. D.. High-order Harmonic Generation in Intense Laser and Magnetic fields. *J Nonlinear Optic Phys Mat* (1995) 04:533, 546. doi:10.1142/s0218863595000227
33. Bandrauk AD, and Lu HZ. Controlling Harmonic Generation in Molecules with Intense Laser and Static Magnetic fields: Orientation Effects. *Phys Rev A* (2003) 68:043408. doi:10.1103/physreva.68.043408
34. Long S., Becker W., and McIver J. K.. Model Calculations of Polarization-dependent Two-Color High-Harmonic Generation. *Phys Rev A* (1995) 52:2262, 2278. doi:10.1103/physreva.52.2262
35. Milošević DB, Becker W, and Kopold R. Generation of Circularly Polarized High-Order Harmonics by Two-Color Coplanar Field Mixing. *Phys Rev A* (2000) 61:063403.
36. Fleischer A., Kfir O., Diskin T., Sidorenko P., and Cohen O.. Spin Angular Momentum and Tunable Polarization in High-Harmonic Generation. *Nature Photon* (2014) 8:543, 549. doi:10.1038/nphoton.2014.108
37. Medišauskas L, Wragg J, van der Hart H, and Ivanov MY. Generating Isolated Elliptically Polarized Attosecond Pulses Using Bichromatic Counterrotating Circularly Polarized Laser fields. *Phys Rev Lett* (2015) 115:153001. doi:10.1103/PhysRevLett.115.153001
38. Milošević DB. Circularly Polarized High Harmonics Generated by a Bicircular Field from Inert Atomic Gases in the P State: A Tool for Exploring Chirality-Sensitive Processes. *Phys Rev A* (2015) 92:043827.
39. Chang Z. Single Attosecond Pulse and Xuv Supercontinuum in the High-Order Harmonic Plateau. *Phys Rev A* (2004) 70:043802. doi:10.1103/physreva.70.043802
40. Mancuso CA, Hickstein DD, Grychtol P, Knut R, Kfir O, Tong X-M, et al. Strong-field Ionization with Two-Color Circularly Polarized Laser fields. *Phys Rev A* (2015) 91:031402(R). doi:10.1103/physreva.91.031402
41. Ngoko Djiokap JM, Hu SX, Madsen LB, Manakov NL, Meremianin AV, and Starace AF. Electron Vortices in Photoionization by Circularly Polarized Attosecond Pulses. *Phys Rev Lett* (2015) 115:113004. doi:10.1103/physrevlett.115.113004
42. Ngoko Djiokap JM, Meremianin AV, Manakov NL, Hu SX, Madsen LB, and Starace AF. Multistart Spiral Electron Vortices in Ionization by Circularly Polarized UV Pulses. *Phys Rev A* (2016) 91:013408.
43. Li M., Zhang G., Kong X., Wang T., Ding X., and Yao J.. Dynamic Stark Induced Vortex Momentum of Hydrogen in Circular fields. *Opt Express* (2018) 26:878. doi:10.1364/oe.26.000878
44. Yuan KJ, Chelkowski S, and Bandrauk AD. Photoelectron Momentum Distributions of Molecules in Bichromatic Circularly Polarized Attosecond UV Laser fields. *Phys Rev A* (2016) 93:053425. doi:10.1103/physreva.93.053425
45. Yuan K.-J., Lu H., and Bandrauk A. D.. Photoionization of triatomic molecular ions H_3^{2+} by intense bichromatic circularly polarized attosecond UV laser pulses. *J Phys B At Mol Opt Phys* (2017) 50:124004. doi:10.1088/1361-6455/aa72fa
46. Ngoko Djiokap JM, Meremianin AV, Manakov NL, Madsen LB, Hu SX, and Starace AF. Dynamical Electron Vortices in Attosecond Double Photoionization of H. *Phys Rev A* (2018) 98:063407. doi:10.1103/physreva.98.063407
47. Pengel D, Kerbstadt S, Johannmeyer D, Englert L, Bayer T, and Wollenhaupt M. Electron Vortices in Femtosecond Multiphoton Ionization. *Phys Rev Lett* (2017) 118:053003. doi:10.1103/physrevlett.118.053003
48. Pengel D, Kerbstadt S, Englert L, Bayer T, and Wollenhaupt M. Control of Three-Dimensional Electron Vortices from Femtosecond Multiphoton Ionization. *Phys Rev A* (2017) 96:043426. doi:10.1103/physreva.96.043426
49. Hasovic E, Becker W, and Milosevic DB. Electron Rescattering in a Bicircular Laser Field. *Opt Express* (2016) 24:6413.
50. Mancuso CA, Hickstein DD, Dorney KM, Ellis JL, Hasovic E, Knut R, et al. Controlling Electron-Ion Rescattering in Two-Color Circularly Polarized Femtosecond Laser fields. *Phys Rev A* (2016) 93:053406. doi:10.1103/physreva.93.053406
51. Li M, Jiang W-C, Xie H, Luo S, Zhou Y, and Lu P. Strong-field Photoelectron Holography of Atoms by Bicircular Two-Color Laser Pulses. *Phys Rev A* (2018) 97:023415. doi:10.1103/physreva.97.023415
52. Yuan KJ, and Bandrauk AD. Above-threshold Ionization in Molecules by Intense Multiple-Frequency Circularly Polarized Laser Pulses. *Phys Rev A* (2018) 98:023413. doi:10.1103/physreva.98.023413
53. Xie X, Scrinzi A, Wickenhauser M, Baltuška A, Barth I, and Kitzler M. Internal Momentum State Mapping Using High Harmonic Radiation. *Phys Rev Lett* (2008) 101:033901. doi:10.1103/physrevlett.101.033901
54. Yuan KJ, and Bandrauk AD. Single Circularly Polarized Attosecond Pulse Generation by Intense Few Cycle Elliptically Polarized Laser Pulses and Terahertz fields from Molecular media. *Phys Rev Lett* (2013) 110:023003. doi:10.1103/physrevlett.110.023003
55. Hernández-García C, Durfee CG, Hickstein DD, Popmintchev T, Meier A, Murnane MM, et al. Schemes for Generation of Isolated Attosecond Pulses of

Pure Circular Polarization. *Phys Rev A* (2016) 93:043855. doi:10.1103/physreva.93.043855
56. Yuan KJ, and Bandrauk AD. Attosecond-magnetic-field-pulse Generation by Electronic Currents in Bichromatic Circularly Polarized UV Laser fields. *Phys Rev A* (2015) 92:063401. doi:10.1103/physreva.92.063401
57. Guo J, Yuan KJ, Lu H, and Bandrauk AD. Spatiotemporal Evolution of Ultrafast Magnetic Field Generation in Molecules with Intense Bichromatic Circularly Polarized Uv Laser Pulses. *Phys Rev A* (2019) 99:053416. doi:10.1103/physreva.99.053416
58. Sederberg S, Kong F, and Corkum PB. Tesla-scale Terahertz Magnetic Impulses. *Phys Rev X* (2020) 10:011063. doi:10.1103/physrevx.10.011063
59. Bandrauk A. D., and Shen H. Exponential split operator methods for solving coupled time-dependent Schrödinger equations. *The Journal of Chemical Physics* (1993) 99:1185, 1193. doi:10.1063/1.465362
60. Bandrauk A. D., and Lu H. Exponential Propagators (Integrators) for the Time-dependent Schrödinger Equation. *J Theor Comput Chem* (2013) 12:1340001. doi:10.1142/s0219633613400014
61. Jefimenko OD. *Electricity and Magnetism: An Introduction to the Theory of Electric and Magnetic Fields*. 2nd ed. Star City, West Virginia: Electret Scientific Co. (1989)
62. Yuan KJ, and Bandrauk AD. Symmetry in Circularly Polarized Molecular High-Order Harmonic Generation with Intense Bicircular Laser Pulses. *Phys Rev A* (2018) 97:023408. doi:10.1103/physreva.97.023408
63. Yuan K.-J., and Bandrauk A. D. Time-resolved Photoelectron Imaging of Molecular Coherent Excitation and Charge Migration by Ultrashort Laser Pulses. *J Phys Chem A* (2018) 122:2241, 2249. doi:10.1021/acs.jpca.7b11669
64. Yuan K.-J., Shu C.-C., Dong D., and Bandrauk A. D. Attosecond Dynamics of Molecular Electronic Ring Currents. *J Phys Chem Lett* (2017) 8:2229, 2235. doi:10.1021/acs.jpclett.7b00877
65. Sharp T. E. Potential-energy curves for molecular hydrogen and its ions. *Atomic Data and Nuclear Data Tables* (1970) 2:119, 169. doi:10.1016/s0092-640x(70)80007-9
66. Juan KJ, Guo J, and Bandrauk AD. Circularly Polarized Attosecond Pulse Generation and Applications to Ultrafast Magnetism. *J Opt* (2017) 19:124016.
67. Yuan K.-J., and Bandrauk A. D. *Applied Sciences* (2019) Probing Attosecond Electron Coherence in Molecular Charge Migration by Ultrafast X-Ray Photoelectron Imaging 9:1941. doi:10.3390/app9091941
68. Corkum P. B., Burnett N. H., and Brunel F. Above-threshold Ionization in the Long-Wavelength Limit. *Phys Rev Lett* (1989) 62:1259, 1262. doi:10.1103/physrevlett.62.1259
69. Corkum P. B. Plasma Perspective on strong Field Multiphoton Ionization. *Phys Rev Lett* (1993) 71:1994, 1997. doi:10.1103/physrevlett.71.1994
70. Yuan KJ, Guo J, and Bandrauk AD. Generation of Ultrafast Magnetic fields from Molecular Coherent Electron Currents. *Phys Rev A* (2018) 98:043410. doi:10.1103/physreva.98.043410
71. Xiao X R, Wang M X, Liang H, Gong Q, and Peng L-Y. Proposal for Measuring Electron Displacement Induced by a Short Laser Pulse. *Phys Rev Lett* (2019) 122:053201. doi:10.1103/physrevlett.122.053201
72. Keldysh LV. Ionization in the Field of a strong Electromagnetic Wave. *Sov Phys JETP* (1965) 20:1307.
73. Mineo H., and Fujimura Y. Quantum Design of π-Electron Ring Currents in Polycyclic Aromatic Hydrocarbons: Parallel and Antiparallel Ring Currents in Naphthalene. *J Phys Chem Lett* (2017) 8:2019, 2025. doi:10.1021/acs.jpclett.7b00704
74. Pronin EA, Starace AF, Frolov MV, and Manakov NL. Perturbation Theory Analysis of Attosecond Photoionization. *Phys Rev A* (2009) 80:063403. doi:10.1103/physreva.80.063403
75. Pronin EA, Starace AF, and Peng LY. Perturbation-theory Analysis of Ionization by a Chirped Few-Cycle Attosecond Pulse. *Phys Rev A* (2011) 84:013417. doi:10.1103/physreva.84.013417
76. Yuan K-J, and Bandrauk AD. Molecular Above-Threshold-Ionization Angular Distributions with Attosecond Bichromatic Intense XUV Laser Pulses. *Phys Rev A* (2012) 85:013413. doi:10.1103/physreva.85.013413
77. Bakos J., Kiss A., Szabó L., and Tendler M. Light Intensity Dependence of the Multiphoton Ionization Probability in the Resonance Case. *Physics Letters A* (1972) 41:163, 164. doi:10.1016/0375-9601(72)91095-x
78. Agostini P., and Bensoussan P. Resonant three-photon ionization of potassium with circularly and linearly polarized light. *Appl Phys Lett* (1974) 24:216, 219. doi:10.1063/1.1655158
79. Yuan K.-J., and Bandrauk A. D. Exploring Coherent Electron Excitation and Migration Dynamics by Electron Diffraction with Ultrashort X-ray Pulses. *Phys Chem Chem Phys* (2017) 19:25846, 25852. doi:10.1039/c7cp05067d
80. Yuan K.-J., and Bandrauk A. D. Ultrafast X-ray Photoelectron Imaging of Attosecond Electron Dynamics in Molecular Coherent Excitation. *J Phys Chem A* (2019) 123:1328, 1336. doi:10.1021/acs.jpca.8b12313
81. Leone S. R., McCurdy C. W., Burgdörfer J., Cederbaum L. S., Chang Z., Dudovich N., et al. What will it take to observe processes in 'real time'? *Nature Photon* (2014) 8:162, 166. doi:10.1038/nphoton.2014.48
82. Kraus PM, Mignolet B, Baykusheva D, Rupenyan A, Horný L, Penka EF, et al. Measurement and Laser Control of Attosecond Charge Migration in Ionized Iodoacetylene. *Science* (2015) 350:790, 5. doi:10.1126/science.aab2160
83. Bandrauk AD, Chelkowski S, Corkum PB, Manz J, and Yudin GL. Attosecond Photoinization of Coherent Superpositions of Bound-Dissociative Molecular States-Effects of Nuclear Motion. *J Phys* (2009) B42:143001.
84. Jia D., Manz J., and Yang Y. De- and Recoherence of Charge Migration in Ionized Iodoacetylene. *J Phys Chem Lett* (2019) 10:4273, 4277. doi:10.1021/acs.jpclett.9b01687
85. Paramonov GK, Klamroth T, Lu HZ, and Bandrauk AD. Quantum Dynamic Isotope Effects and Power Spectra of H2+ and HD+ in Strong One-Cycle Laser Pulses". *Phys Rev* (2018) A98:063431.
86. Zhu BJ, et al. 30 Co-authors), Strong Magnetic fields with Simple Coils Irradiated by High Power Lasers. *Appl Phys Lett* (2015) 107:2619003. doi:10.1063/1.4939119

Conflict of Interest: The authors declare that the research was conducted in the absence of any commercial or financial relationships that could be construed as a potential conflict of interest.